



Combined Upper Limits on Standard Model Higgs Boson Production from the DØ Experiment in 0.9–5.0 fb⁻¹

The DØ Collaboration
URL <http://www-d0.fnal.gov>
(Dated: August 14, 2009)

Searches for standard model Higgs boson production in $p\bar{p}$ collisions at $\sqrt{s} = 1.96$ TeV have been carried out for Higgs boson masses (m_H) in the range $100 < m_H < 200$ GeV/ c^2 . The contributing production processes include associated production ($q\bar{q} \rightarrow W/ZH$), gluon fusion ($gg \rightarrow H$), and vector boson fusion ($q\bar{q} \rightarrow q'\bar{q}'H$). Analyses are conducted with integrated luminosities from 0.9 fb⁻¹ to 5.0 fb⁻¹. As no significant excess is observed, we proceed to set limits on standard model Higgs boson production. The observed 95% confidence level upper limits are found to be a factor of 3.2 (1.3) higher than the predicted standard model cross section at $m_H = 115$ (165) GeV/ c^2 while the expected limits are found to be a factor of 3.1 (1.7) higher than the standard model cross section for the same masses.

I. INTRODUCTION

Despite its success as a predictive tool, the standard model (SM) of particle physics remains incomplete without a means to explain electroweak symmetry breaking. The simplest proposed mechanism involves the introduction of a complex doublet of scalar fields that generate the masses of elementary particles via their mutual interactions. After accounting for longitudinal polarizations for the electroweak bosons, this so-called Higgs mechanism also gives rise to a single scalar boson with an unpredicted mass. Direct searches in $e^+e^- \rightarrow Z^* \rightarrow ZH$ at the Large Electron Positron (LEP) collider yielded lower mass limits at $m_H > 114.4 \text{ GeV}/c^2$ [1] while precision electroweak data yield the indirect constraint $m_H < 163 \text{ GeV}/c^2$ [2], with both limits set at 95% confidence level (C.L.). When also considering the direct limit, the indirect constraint predicts $m_H < 191 \text{ GeV}/c^2$, indicating that the range $110 \leq m_H \leq 200 \text{ GeV}/c^2$ is the most important search region for a SM Higgs boson. The search for a SM Higgs boson is one of the main goals of the Fermilab Tevatron physics program.

In this note, we combine the results of direct searches for SM Higgs bosons in $p\bar{p}$ collisions at $\sqrt{s} = 1.96 \text{ TeV}$ recorded by the $D\bar{O}$ experiment [3]. The analyses combined here seek signals of Higgs bosons produced in association with vector bosons ($q\bar{q} \rightarrow W/ZH$), through gluon-gluon fusion (GGF) ($gg \rightarrow H$), and through vector boson fusion (VBF) ($q\bar{q} \rightarrow q'\bar{q}'H$) corresponding to integrated luminosities ranging from 0.9 to 5.0 fb^{-1} , collected during the period 2002–2009. The Higgs boson decay modes studied are $H \rightarrow b\bar{b}$, $H \rightarrow W^+W^-$, $H \rightarrow \tau^+\tau^-$ and $H \rightarrow \gamma\gamma$. The searches are organized into 61 analysis subsets comprising different production, decay and final state particle configurations, each designed to isolate a particular Higgs boson production and decay mode. In order to facilitate proper combination of signals, the analyses were designed to be mutually exclusive after analysis selections. Searches for several final states are performed in two distinct epochs of data collection: before and after the 2006 $D\bar{O}$ detector upgrade. The largest changes made during the upgrade were the addition of a new layer to the silicon detector nearest to the beam-line and an upgrade of the trigger system. The two epochs are denoted as Run IIa (1.1 fb^{-1}) and Run IIb (still on-going, currently up to 3.9 fb^{-1} are analyzed in this note).

The 61 analyses used in this combination [4–14] are outlined in Table I. In the cases of $p\bar{p} \rightarrow W/ZH + X$ production, we search for a Higgs boson decaying to two bottom quarks, or two tau leptons. The decays of the vector bosons further define the analyzed final states. To isolate $H \rightarrow b\bar{b}$ decays, an algorithm for identifying jets consistent with the decay of a heavy-flavor quark is applied to each jet (b -tagging). Several kinematic variables sensitive to transversely-displaced jet vertices and jet tracks with large transverse impact parameters relative to the hard-scatter vertices are combined in a neural network (NN) discriminant trained to identify heavy-flavor quark decays and reject jets arising from light-flavor quarks or gluons [15]. By adjusting a minimum requirement on the b -tagging NN output, a spectrum of increasingly stringent b -tagging operating points is achieved, each with a different signal efficiency and purity. For the $WH \rightarrow \ell\nu b\bar{b}$ and $ZH \rightarrow \ell\bar{\ell} b\bar{b}$ processes, the analyses are separated into two groups: one in which two of the jets were b -tagged with a loose tagging requirement (herein called double b -tag or DT) and one group in which only one jet was tagged with a tight tag algorithm (single b -tag or ST). The ST selection excludes additional loose-tagged jets, rendering the ST and DT selections orthogonal. The ST selection results in a typical per-jet efficiency and fake rate of about 50% and 0.5%, while the DT selection gives 60% and 1.5%. For these analyses, each lepton flavor of the W/Z boson decay ($\ell = e, \mu$) is treated as an independent channel. For the $ZH \rightarrow \nu\bar{\nu} b\bar{b}$ analyses, two or three jets are required in the final state with the two leading jets satisfying a loose b -tag and one of these jets also satisfying a tight b -tag. In the case of $WH \rightarrow \ell\nu b\bar{b}$ production, the primary lepton from the W boson decay may fall outside of the detector fiducial volume or is not identified. Events of this type are selected by the $ZH \rightarrow \nu\bar{\nu} b\bar{b}$ analysis. A similar scenario is possible in which one τ lepton is lost in $ZH \rightarrow \tau\tau b\bar{b}$ decays. This signature is detected in the $WH \rightarrow \tau\nu b\bar{b}$ analysis. The $t\bar{t}H \rightarrow t\bar{t} b\bar{b}$ search channel analyses final states with up to 3 b -tags where in addition to the $H \rightarrow b\bar{b}$ decay b -jets emerge due to top quark decays.

We also consider Higgs decays to two W^\pm bosons. For $WH \rightarrow WW^+W^-$ production, we search for leptonic W boson decays with three final states of same-signed leptons: $WWW \rightarrow e^\pm\nu e^\pm\nu + X$, $e^\pm\nu\mu^\pm\nu + X$, and $\mu^\pm\nu\mu^\pm\nu + X$. In the case of $p\bar{p} \rightarrow H \rightarrow W^+W^-$ and $p\bar{p} \rightarrow q\bar{q}H \rightarrow q\bar{q}W^+W^-$ production via vector boson fusion, we search for leptonic W boson decays with three final states of opposite-signed leptons: $WWW \rightarrow e^+\nu e^-\nu$, $e^\pm\nu\mu^\mp\nu$, and $\mu^+\nu\mu^-\nu$. In addition we also consider final states originating from Higgs boson production in association with a vector boson (WH or ZH), where leptons may originate from the vector boson or Higgs boson decay, excluding events which are considered in the Higgs search in the Wbb and Zbb final states. For the gluon fusion and vector boson fusion processes, $H \rightarrow b\bar{b}$ decays are not considered due to the large multijet background. In all $H \rightarrow W^+W^-$ decays with $m_H < 2M_W$, one of the W bosons will be off mass shell. In all cases, lepton selections include both electrons and muons ($\ell = e, \mu$), while τ leptons are included in the simulation and the selections necessarily have acceptance for secondary leptons from $\tau \rightarrow e\nu, \mu\nu$ decays. Finally, we include an analysis that searches for Higgs bosons decaying to two photons and produced via gluon-gluon fusion, vector boson fusion, and associated production mechanisms.

Since the most recent $D\bar{O}$ SM combined Higgs boson search results [16], we have updated the $WH \rightarrow \ell\nu b\bar{b}$ analysis and the $H + X \rightarrow \tau\tau b\bar{b}/q\bar{q}\tau\tau$ analysis. (The second selects the $\tau\tau +$ dijet final state with one τ decaying to μ and the

other decaying hadronically. This analysis is sensitive to $ZH \rightarrow \tau\tau b\bar{b}$, $W/ZH \rightarrow q\bar{q}\tau\tau$, GGF and VBF.)

TABLE I: List of analysis channels, corresponding integrated luminosities, and final variables. See Sect. I for details. The final variable used for several analyses is a neural-network or boosted decision-tree discriminant output which is abbreviated as “NN discriminant” and “DTree discriminant”, respectively.

Channel	Data Epoch	Luminosity (fb^{-1})	Final Variable	# Sub-Channels	Reference
$WH \rightarrow \ell\nu b\bar{b}$, ST/DT, $W+2$ jet	Run IIa+Run IIb	5.0	NN discriminant	8	[4]
$WH \rightarrow \ell\nu b\bar{b}$, ST/DT, $W+3$ jet	Run IIa+Run IIb	5.0	Dijet Mass	8	[4]
$WH \rightarrow \tau\nu b\bar{b}$	Run IIa	0.9	Dijet Mass	5	[5]
$H+X \rightarrow \tau\tau b\bar{b}/q\bar{q}\tau\tau$	Run IIa	1.0	NN discriminant	1	[5]
$H+X \rightarrow \tau\tau b\bar{b}/q\bar{q}\tau\tau$	Run IIb	3.9	DTree discriminant	1	[6]
$ZH \rightarrow \nu\bar{\nu} b\bar{b}$, DT	Run IIa+Run IIb	2.1	DTree discriminant	2	[7]
$ZH \rightarrow e^+e^- b\bar{b}$, ST/DT	Run IIa	1.1	NN discriminant	2	[8]
$ZH \rightarrow \mu^+\mu^- b\bar{b}$, ST/DT	Run IIa	1.1	NN discriminant	2	[8]
$ZH \rightarrow e^+e^- b\bar{b}$, ST/DT	Run IIb	3.1	DTree discriminant	6	[9]
$ZH \rightarrow \mu^+\mu^- b\bar{b}$, ST/DT	Run IIb	3.1	DTree discriminant	2	[9]
$ZH \rightarrow \mu^\pm + \text{track } b\bar{b}$, ST/DT	Run IIa+Run IIb	4.2	DTree discriminant	2	[9]
$WH \rightarrow WW^+W^-$	Run IIa	1.1	2-D Likelihood	3	[10]
$WH \rightarrow WW^+W^-$	Run IIb	2.5	1-D Likelihood	3	[11]
$H \rightarrow W^+W^- (\mu^+\mu^-)$	Run IIa+Run IIb	3.0	NN discriminant	1	[12]
$H \rightarrow W^+W^- (e^\pm\mu^\mp)$	Run IIa+Run IIb	4.2	NN discriminant	1	[12]
$H \rightarrow W^+W^- (e^+e^-)$	Run IIa+Run IIb	4.2	NN discriminant	1	[12]
$H \rightarrow \gamma\gamma$	Run IIa+Run IIb	4.2	Di-photon Mass	1	[13]
$t\bar{t}H \rightarrow t\bar{t}b\bar{b}$	Run IIa+Run IIb	2.1	Scaled H_T	12	[14]

All Higgs boson signals are simulated using PYTHIA [17], and CTEQ5L or CTEQ6L [18] leading-order (LO) parton distribution functions. The associated production and VBF Higgs signal production cross sections are normalized to next-to-next-to-leading-order (NNLO) calculations [19–21]. The $gg \rightarrow H$ production cross sections are calculated at NNLL in QCD, treat the bottom quark contribution to NLO, and also includes two-loop electroweak effects [22]. The $gg \rightarrow H$ production cross section depends strongly on the PDF set chosen and the accompanying value of α_s . The calculation we use [22] is made with the MSTW 2008 NNLO PDF set [23]. These supercede the cross sections used in the update of Summer 2008 [19, 24]. The newer cross sections include a more thorough treatment of higher-order radiative corrections, particularly those involving b quark loops, as well as using the MSTW 2008 PDF set instead of the MRST 2002 PDF set [25]. The Higgs boson production cross sections used for this process are listed in Table II. The Higgs boson decay branching ratio predictions are calculated with HDECAY [26].

The contributions from multijet production are measured in data. The other backgrounds were generated by PYTHIA, ALPGEN [27], and COMPHEP [28], with PYTHIA providing parton-showering and hadronization. Background cross sections are either normalized to next-to-leading order (NLO) calculations from MCFM [29] or to data control samples whenever possible.

II. LIMIT CALCULATIONS

We combine results using the CL_s method with a negative log-likelihood ratio (LLR) test statistic [30]. The value of CL_s is defined as $CL_s = CL_{s+b}/CL_b$ where CL_{s+b} and CL_b are the confidence levels for the signal-plus-background hypothesis and the background-only hypothesis, respectively. These confidence levels are evaluated by integrating corresponding LLR distributions populated by simulating outcomes via Poisson statistics. Separate channels and bins are combined by summing LLR values over all bins and channels. This method provides a robust means of combining individual channels while maintaining individual channel sensitivities and incorporating systematic uncertainties. Systematics are treated as Gaussian uncertainties on the expected number of signal and background events, not the outcomes of the limit calculations. This approach ensures that the uncertainties and their correlations are propagated to the outcome with their proper weights. The CL_s approach used in this analysis utilizes binned final-variable distributions rather than a single-bin (fully integrated) value for each contributing analysis. The exclusion criteria are determined by increasing the signal cross section until $CL_s = 1 - \alpha$, which defines a signal cross section excluded at 95% confidence level for $\alpha = 0.95$.

TABLE II: The (N)NLO production cross sections and decay branching fractions for the SM Higgs boson assumed for the combination of channels.

m_H (GeV/ c^2)	$\sigma_{gg \rightarrow H}$ (fb)	σ_{WH} (fb)	σ_{ZH} (fb)	σ_{VBF} (fb)	$B(H \rightarrow b\bar{b})$ (%)	$B(H \rightarrow \tau^+\tau^-)$ (%)	$B(H \rightarrow W^+W^-)$ (%)	$B(H \rightarrow \gamma\gamma)$
100	1861	286.1	166.7	99.5	81.21	7.924	1.009	$0.153 \cdot 10^{-2}$
105	1618	244.6	144.0	93.3	79.57	7.838	2.216	$0.171 \cdot 10^{-2}$
110	1413	209.2	124.3	87.1	77.02	7.656	4.411	$0.190 \cdot 10^{-2}$
115	1240	178.8	107.4	79.07	73.22	7.340	7.974	$0.206 \cdot 10^{-2}$
120	1093	152.9	92.7	71.65	67.89	6.861	13.20	$0.219 \cdot 10^{-2}$
125	967	132.4	81.1	67.37	60.97	6.210	20.18	$0.225 \cdot 10^{-2}$
130	858	114.7	70.9	62.5	52.71	5.408	28.69	$0.223 \cdot 10^{-2}$
135	764	99.3	62.0	57.65	43.62	4.507	38.28	$0.212 \cdot 10^{-2}$
140	682	86.0	54.2	52.59	34.36	3.574	48.33	$0.194 \cdot 10^{-2}$
145	611	75.3	48.0	49.15	25.56	2.676	58.33	$0.169 \cdot 10^{-2}$
150	548	66.0	42.5	45.67	17.57	1.851	68.17	$0.139 \cdot 10^{-2}$
155	492	57.8	37.6	42.19	10.49	1.112	78.23	$0.103 \cdot 10^{-2}$
160	439	50.7	33.3	38.59	4.00	0.426	90.11	$0.551 \cdot 10^{-3}$
165	389	44.4	29.5	36.09	1.265	0.136	96.10	$0.217 \cdot 10^{-3}$
170	349	38.9	26.1	33.58	0.846	0.091	96.53	$0.150 \cdot 10^{-3}$
175	314	34.6	23.3	31.11	0.663	0.072	95.94	$0.121 \cdot 10^{-3}$
180	283	30.7	20.8	28.57	0.541	0.059	93.45	$0.102 \cdot 10^{-3}$
185	255	27.3	18.6	26.81	0.420	0.046	83.79	$0.807 \cdot 10^{-4}$
190	231	24.3	16.6	24.88	0.342	0.038	77.61	$0.671 \cdot 10^{-4}$
195	210	21.7	15.0	23.00	0.295	0.033	74.95	$0.587 \cdot 10^{-4}$
200	192	19.3	13.5	21.19	0.260	0.029	73.47	$0.525 \cdot 10^{-4}$

A. Final Variable Preparation

For the $WH \rightarrow \ell\nu b\bar{b}$, Run IIa $H+X \rightarrow \tau\tau b\bar{b}/q\bar{q}\tau\tau$, Run IIa $ZH \rightarrow \ell\ell b\bar{b}$, and $H \rightarrow W^+W^-$ analyses, the final variable used for limit setting is the output of a neural-network (NN) discriminant, trained separately for each Higgs boson mass tested, except for the $WH \rightarrow \ell\nu b\bar{b}/W + 3$ jet and $WH \rightarrow \tau\nu b\bar{b}$ analyses, where the dijet invariant mass is used. The Run IIa(b) $WH \rightarrow WW^+W^-$ analyses utilize a two(one)-dimensional likelihood discriminant as a final variable. The $ZH \rightarrow \nu\bar{\nu} b\bar{b}$, Run IIb $H+X \rightarrow \tau\tau b\bar{b}/q\bar{q}\tau\tau$, and Run IIb $ZH \rightarrow \ell\ell b\bar{b}$ analyses all employ separate boosted decision-tree (DTree) discriminants. The $H \rightarrow \gamma\gamma$ analysis uses the diphoton invariant mass. The $t\bar{t}H \rightarrow t\bar{t} b\bar{b}$ analysis uses a scaled sum of transverse jet momenta (scaled H_T) as a final variable. The final variables for all analyses are shown in Figs. 1-4. In many of these figures, multiple contributing sub processes of common sources are summed together.

Most of the analyses are performed on a fine Higgs boson mass grid (every 5 GeV/ c^2). For those on a 10 GeV/ c^2 grid, additional mass points are created via interpolation of signals and backgrounds [31].

B. Systematic Uncertainties

The systematic uncertainties differ between analyses for both the signals and backgrounds [4–14]. Here we will summarize only the largest contributions. Most analyses carry an uncertainty on the integrated luminosity of 6.1%, while the overall normalization of other analyses is determined from the NNLO Z/γ^* cross section in data events near the peak of $Z \rightarrow \ell\ell$ decays. The $H \rightarrow b\bar{b}$ analyses have an uncertainty on the b -tagging rate of 2-6% per tagged jet. These analyses also have an uncertainty on the jet measurement and acceptances of $\sim 7.5\%$. All analyses include uncertainties associated with lepton measurement and acceptances, which range from 3-6% depending on the final state. The largest contribution for all analyses is the uncertainty on the background cross sections at 6-30% depending on the analysis channel and specific background. These values include both the uncertainty on the theoretical cross section calculations and the uncertainties on the higher order correction factors. The uncertainty on the expected multijet background is dominated by the statistics of the data sample from which it is estimated, and is considered separately from the other cross section uncertainties. The $p\bar{p} \rightarrow H \rightarrow W^+W^-$ and $H \rightarrow \gamma\gamma$ analyses also assign a 10% uncertainty to the NNLO Higgs production cross section associated with the accuracy of the theoretical calculation. In addition, several analyses incorporate shape-dependent uncertainties on the kinematics of the dominant backgrounds

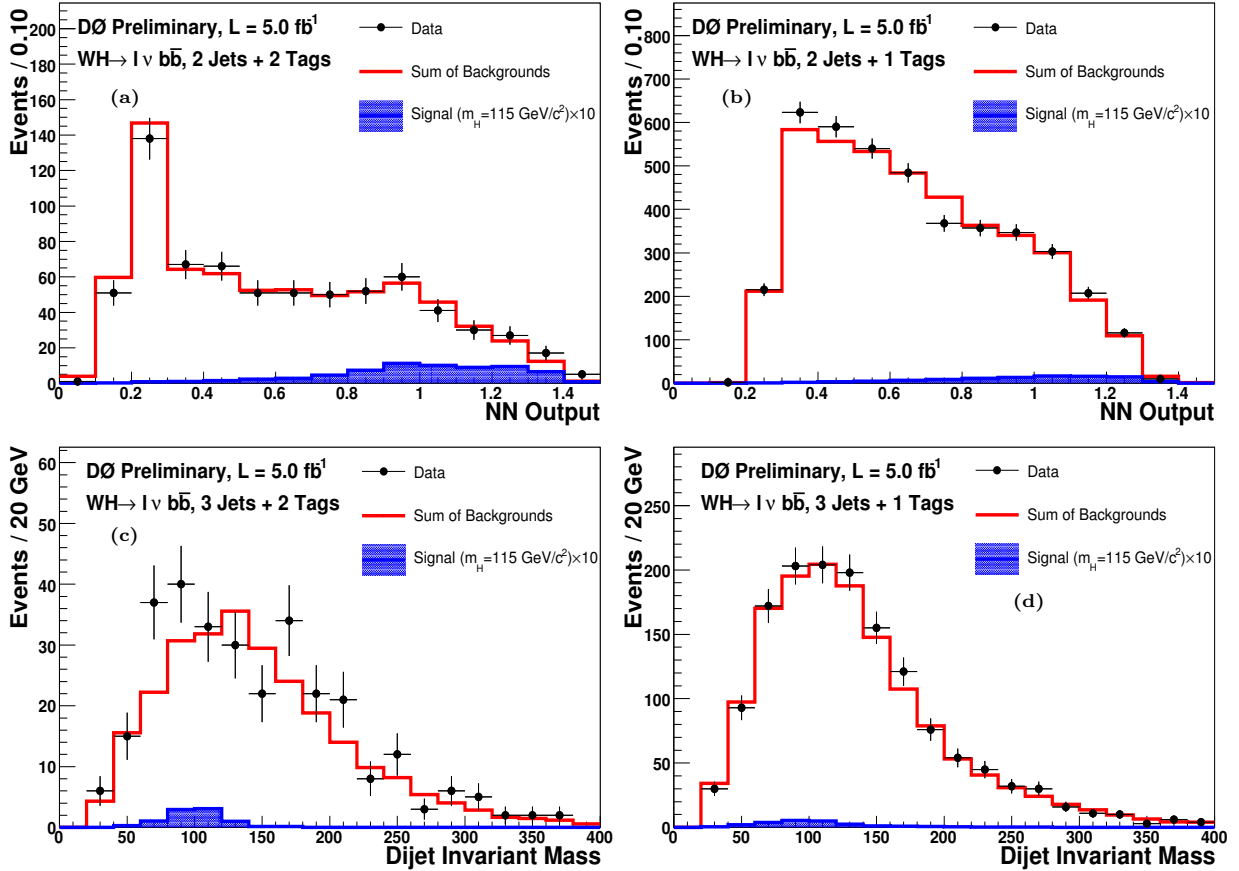


FIG. 1: Final variable distributions for the $pp \rightarrow WH \rightarrow l\nu b\bar{b}$ Higgs search analyses. The figure contains distributions for: the NN discriminant for the $WH \rightarrow l\nu b\bar{b}$ DT 2-jet analyses (a), the NN discriminant for the $WH \rightarrow l\nu b\bar{b}$ ST 2-jet analyses (b), the dijet invariant mass for the $WH \rightarrow l\nu b\bar{b}$ DT 3-jet analyses (c), and the dijet invariant mass for the $WH \rightarrow l\nu b\bar{b}$ ST 3-jet analyses (d). For each figure, the total signal and background expectations and the observed data are shown.

in the analyses. These shapes are derived from the potential deformations of the final variables due to generator and background modeling uncertainties. Further details on the systematic uncertainties are given in Table III.

The systematic uncertainties for background rates are generally several times larger than the signal expectation itself and are an important factor in the calculation of limits. Each systematic uncertainty is folded into the signal and background expectations in the limit calculation via Gaussian distributions. These Gaussian values are sampled for each Poisson MC trial (pseudo-experiment). Several of the systematic uncertainties, for example the jet energy scale uncertainty, typically impact the shape of the final variable. These shape dependences were preserved in the description of systematic fluctuations for each Poisson trial. Correlations between systematic sources are carried through in the calculation. For example, the uncertainty on the integrated luminosity is held to be correlated between all signals and backgrounds and, thus, the same fluctuation in the luminosity is common to all channels for a single pseudo-experiment. All systematic uncertainties originating from a common source are held to be correlated, as detailed in Tables III and IV.

To minimize the degrading effects of systematics on the search sensitivity, the individual background contributions are fitted to the data observation by maximizing a profile likelihood function for each hypothesis [32]. The profile likelihood is constructed via a joint Poisson probability over the number of bins in the calculation and is a function of the nuisance parameters in the system and their associated uncertainties, which are given an additional Gaussian constraint associated with their prior predictions. The maximization of the likelihood function is performed over the nuisance parameters. A fit is performed to both the background-only (b) and signal-plus-background (s+b) hypothesis separately for each Poisson MC trial.

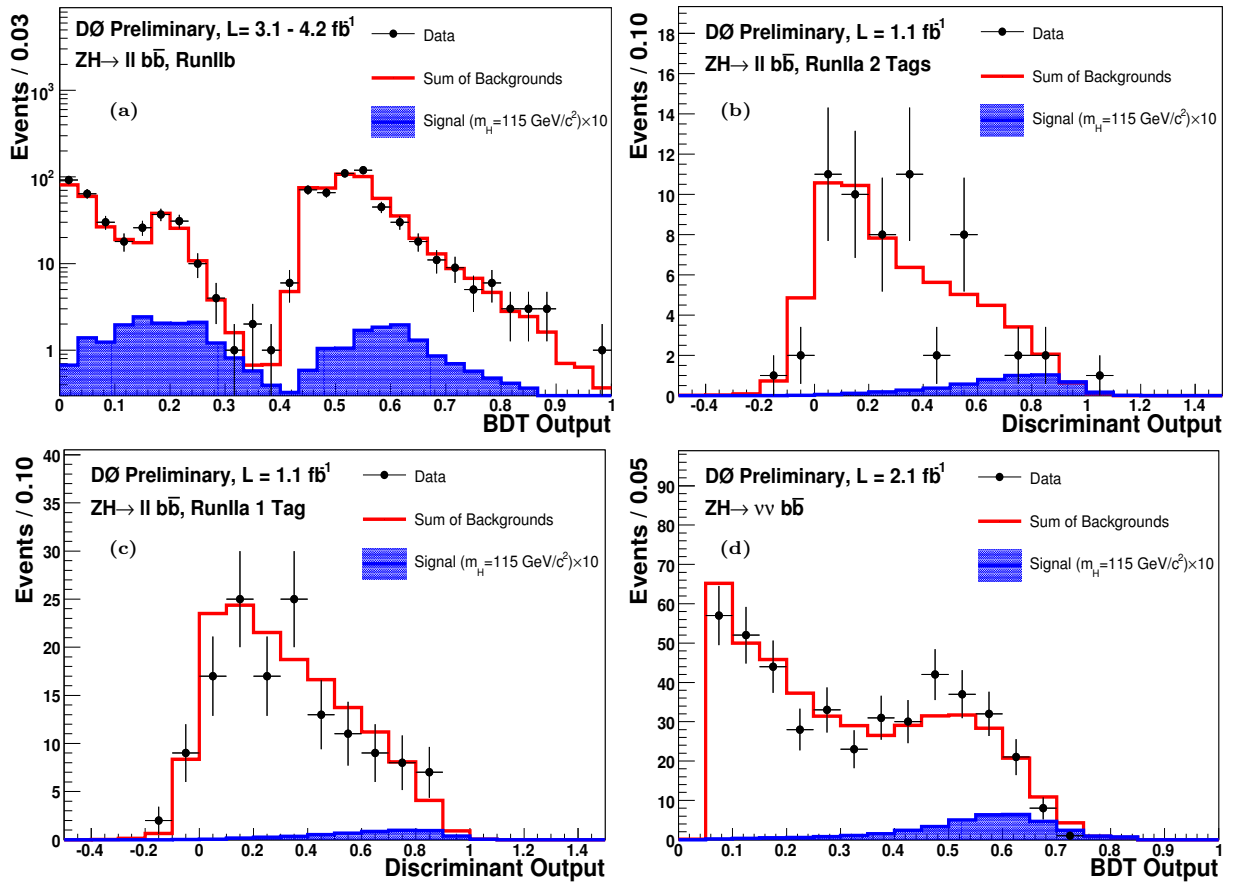


FIG. 2: Final variable distributions for the $p\bar{p} \rightarrow ZH \rightarrow \ell\ell/\nu\nu b\bar{b}$ Higgs search analyses. The figure contains distributions for: the DTree discriminant for the Run I Ib $ZH \rightarrow \ell\ell b\bar{b}$ analyses (the left peak corresponds to the DT selection and the right peak corresponds to the ST selection) (a), the discriminant for the Run I Ia $ZH \rightarrow \ell\ell b\bar{b}$ DT analyses (b), the discriminant for the Run I Ia $ZH \rightarrow \ell\ell b\bar{b}$ ST analysis (c), and the DTree discriminant for the $ZH \rightarrow \nu\nu b\bar{b}$ analyses (d). For each figure, the total signal and background expectations and the observed data are shown.

III. DERIVED UPPER LIMITS

We derive limits on SM Higgs boson production $\sigma \times BR(H \rightarrow b\bar{b}/W^+W^-/\tau^+\tau^-)$ via 61 individual analyses [4–14]. The limits are derived at a 95% C.L. To facilitate model transparency and to accommodate analyses with different degrees of sensitivity, we present our results in terms of the ratio of 95% C.L. upper cross section limits to the SM predicted cross section as a function of Higgs boson mass. The SM prediction for Higgs boson production would therefore be considered excluded at 95% C.L. when this limit ratio falls below unity.

The individual analyses described in Table I are grouped to evaluate combined limits over the range $100 \leq m_H \leq 200 \text{ GeV}/c^2$. The $WH \rightarrow \tau\nu b\bar{b}$, $H+X \rightarrow \tau\tau b\bar{b}/q\bar{q}\tau\tau$ and $ZH \rightarrow \nu\nu b\bar{b}$ analyses contribute to the region $m_H \leq 145 \text{ GeV}/c^2$, the $ZH \rightarrow \ell\ell b\bar{b}$ $WH \rightarrow \nu b\bar{b}$ and $H \rightarrow \gamma\gamma$ analyses contribute for $m_H \leq 150 \text{ GeV}/c^2$, the $WH \rightarrow WW^+W^-$ analyses contribute for $m_H \geq 120 \text{ GeV}/c^2$, the $t\bar{t}H \rightarrow t\bar{t}b\bar{b}$ analysis contributes for $m_H \leq 155 \text{ GeV}/c^2$, and the $H \rightarrow W^+W^-$ analyses contribute for $m_H \geq 115 \text{ GeV}/c^2$.

Figure 5 shows the expected and observed 95% C.L. cross section limit ratio to the SM cross sections for all analyses combined over the probed mass region ($100 \leq m_H \leq 200 \text{ GeV}/c^2$). These results are also summarized in Table V. The LLR distributions for the full combination are shown in Fig. 6. Included in these figures are the median LLR values for the signal-plus-background hypothesis (LLR_{s+b}), background-only hypothesis (LLR_b), and the observed data (LLR_{obs}). The shaded bands represent the 1 and 2 standard deviation (σ) departures for LLR_b . These distributions can be interpreted as follows:

- The separation between LLR_b and LLR_{s+b} provides a measure of the discriminating power of the search. This is the ability of the analysis to separate the $s+b$ and b -only hypotheses.

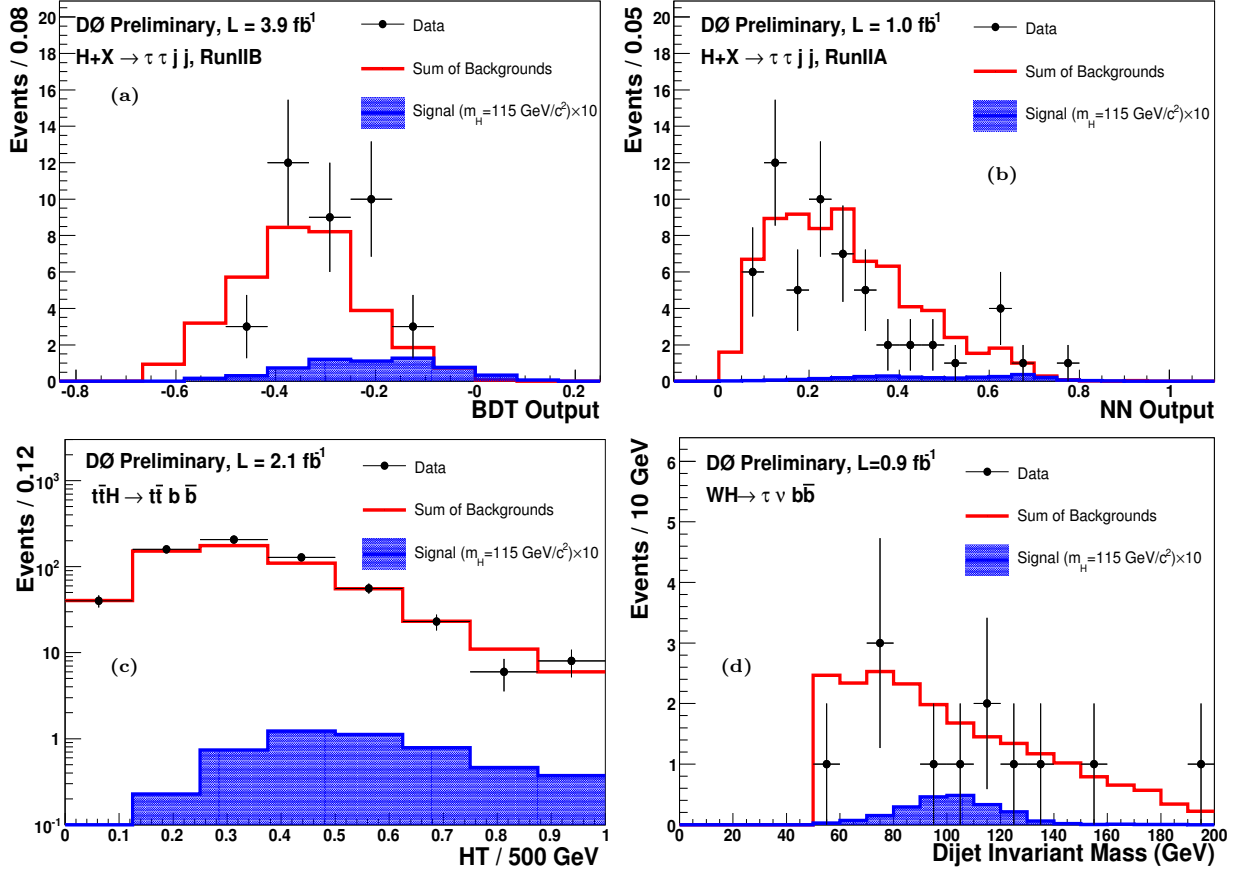


FIG. 3: Final variable distributions for selected Higgs search analyses. The figure contains final variable distributions for: the DTree discriminant for the Run IIB $H+X \rightarrow \tau\tau b\bar{b}/q\bar{q}\tau\tau$ analysis (a), the NN discriminant for the Run IIA $H+X \rightarrow \tau\tau b\bar{b}/q\bar{q}\tau\tau$ analysis (b), the scaled H_T variable for the Run IIA $t\bar{t}H \rightarrow t\bar{t} b\bar{b}$ analyses (c), and the dijet invariant mass for the Run IIA $WH \rightarrow \tau\nu b\bar{b}$ analyses (d). For each figure, the total signal and background expectations and the observed data are shown.

- The width of the LLR_b distribution (shown here as one and two standard deviation (σ) bands) provides an estimate of how sensitive the analysis is to a signal-like background fluctuation in the data, taking account of the presence of systematic uncertainties. For example, when a 1σ background fluctuation is large compared to the signal expectation, the analysis sensitivity is thereby limited.
- The value of LLR_{obs} relative to LLR_{s+b} and LLR_b indicates whether the data distribution appears to be more like signal-plus-background or background-only. As noted above, the significance of any departures of LLR_{obs} from LLR_b can be evaluated by the width of the LLR_b distribution.

IV. CONCLUSIONS

We have presented upper limits on standard model Higgs boson production derived from 61 Higgs search analyses. We have combined these analyses and form new limits more sensitive than each individual limit. The observed (expected) 95% C.L. upper limit ratios to the SM Higgs boson production cross sections are 3.2 (3.1) at $m_H = 115 \text{ GeV}/c^2$ and 1.3 (1.7) at $m_H = 165 \text{ GeV}/c^2$.

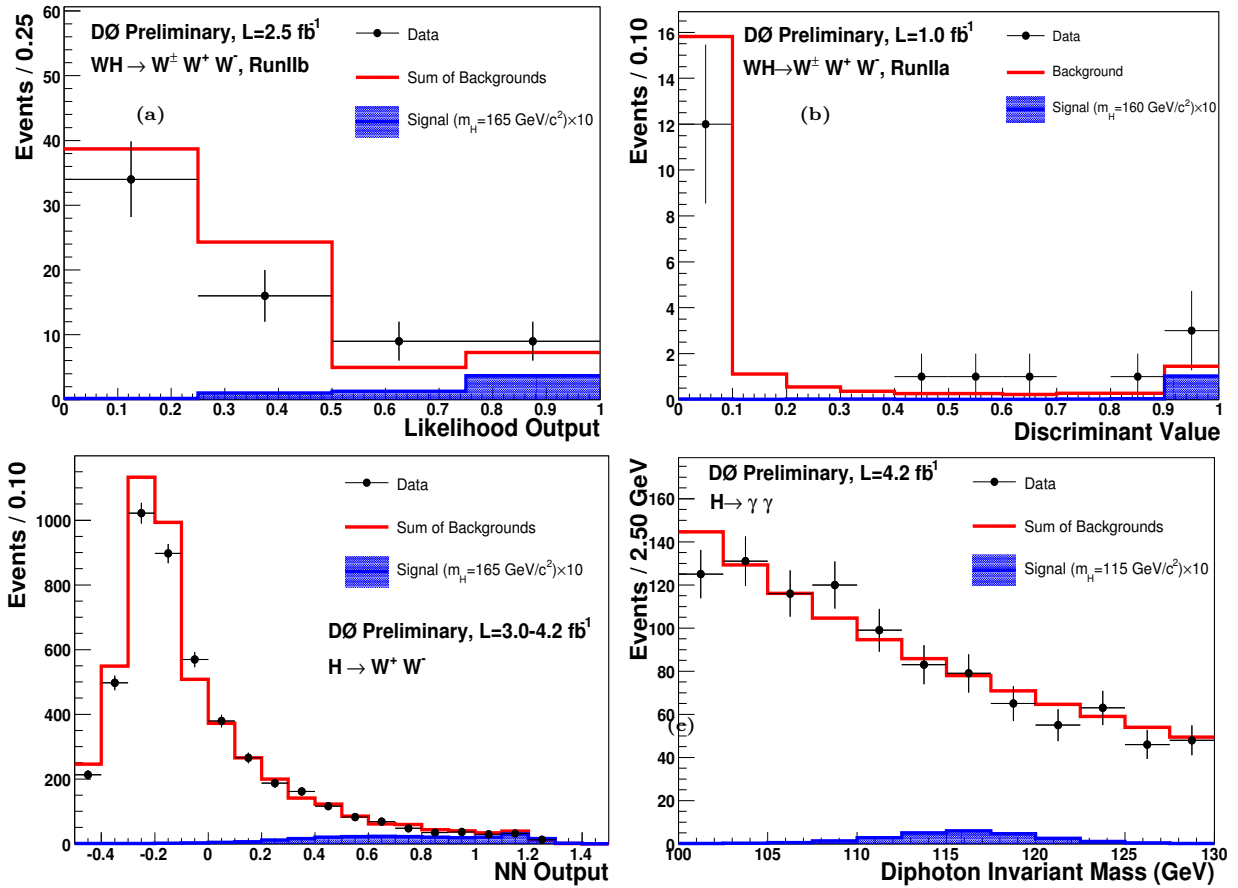


FIG. 4: Final variable distributions for selected Higgs search analyses. The figure contains distributions for: the likelihood discriminant for the Run IIB $WH \rightarrow WW^+W^-$ analysis (a), the likelihood discriminant for the Run IIA $WH \rightarrow WW^+W^-$ analysis (b), the NN discriminant for the $H \rightarrow W^+W^-$ analyses (c) and the diphoton invariant mass for the $H \rightarrow \gamma\gamma$ analysis (d). For each figure, the total signal and background expectations and the observed data are shown.

Acknowledgments

We thank the staffs at Fermilab and collaborating institutions, and acknowledge support from the DOE and NSF (USA), CEA and CNRS/IN2P3 (France), FASI, Rosatom and RFBR (Russia), CNPq, FAPERJ, FAPESP and FUNDUNESP (Brazil), DAE and DST (India), Colciencias (Colombia), CONACyT (Mexico), KRF and KOSEF (Korea), CONICET and UBACyT (Argentina), FOM (The Netherlands), STFC (United Kingdom), MSMT and GACR (Czech Republic), CRC Program, CFI, NSERC and WestGrid Project (Canada), BMBF and DFG (Germany), SFI (Ireland), The Swedish Research Council (Sweden), CAS and CNSF (China), and the Alexander von Humboldt Foundation.

TABLE III: List of leading correlated systematic uncertainties in %. All uncertainties within a group are considered 100% correlated across channels. The correlated systematic uncertainty on the background cross section (σ) and shape-dependent background modeling are themselves subdivided according to the different background processes in each analysis.

Source	$WH \rightarrow e\nu b\bar{b}$	$WH \rightarrow \mu\nu b\bar{b}$	$WH \rightarrow WW^+W^-$	$WH \rightarrow \tau\nu b\bar{b}$
Luminosity	6.1	6.1	-	6.1
Normalization	-	-	6.1	-
Jet Energy Scale	3.0	3.0	-	3.0
Jet ID	5.0	5.0	-	4.0
Jet Triggers	-	-	5.5	-
Tau Energy Scale/ID	-	-	-	7.0
Electron ID/Trigger	4.0	-	11	-
Muon ID/Trigger	-	5.0	11	-
b -Jet Tagging	3-6	3-6	-	4-6
Background σ	6-20	6-20	6-18	6-18
Multijet	14	14	30-50	25
Shape-Dependent Bkgd Modeling	2-10	2-10	-	5-20

Source	$ZH \rightarrow \nu\bar{\nu} b\bar{b}$	$ZH \rightarrow e^+e^- b\bar{b}$	$ZH \rightarrow \mu^+\mu^- b\bar{b}$
Luminosity	6.1	6.1	6.1
Jet Energy Scale	3.0	2.0	2.0
Jet ID	2.0	5.0	5.0
Jet Triggers	5.5	-	-
Electron ID/Trigger	0	4.0	-
Muon ID/Trigger	0	-	4.0
b -Jet Tagging	6.0	3.0-7.5	3.0-7.5
Background σ	6-16	10-30	10-30
Heavy-Flavor Scale	50	-	-
Multijet	-	41-50	50
Shape-Dependent Bkgd Modeling	-	5-10	5-10

Source	$H \rightarrow W^+W^-$	$t\bar{t}H \rightarrow t\bar{t}b\bar{b}$	$H \rightarrow \gamma\gamma$	$H+X \rightarrow \tau\tau b\bar{b}/q\bar{q}\tau\tau$
Luminosity	-	6.1	6.1	6.1
Normalization	4-6	-	-	-
Jet Energy Scale	3.0	-	-	7.5
Jet ID	1-2	-	-	6
Tau Energy Scale/ID	-	-	-	9
Electron ID/Trigger	3-10	2.5	3	-
Muon ID/Trigger	7.7-10	2	-	7
b -Jet Tagging	-	-	-	-
Background σ	6-20	10-15	6	6-20
Signal σ	10	-	10	10
Multijet	5-20	1-5	1	5-40
Shape-Dependent Bkgd Modeling	5-20	-	5-7	-

TABLE IV: The correlation matrix for the analysis channels. All uncertainties within a group are considered 100% correlated across channels. The correlated systematic uncertainty on the background cross section (σ) is itself subdivided according to the different background processes in each analysis.

Source	$WH \rightarrow \ell \nu b \bar{b}$	$ZH \rightarrow \nu \bar{\nu} b \bar{b}$	$ZH \rightarrow \ell \ell b \bar{b}$	$H \rightarrow W^+ W^-$	$WH \rightarrow WW^+ W^-$
Luminosity	×	×	×		
Normalization			×	×	×
Jet Energy Scale	×	×	×	×	
Jet ID	×	×	×		
Tau Energy Scale/ID					
Electron ID/Trigger	×		×	×	×
Muon ID/Trigger	×		×	×	×
b -Jet Tagging	×	×	×		
Background σ	×	×	×	×	×
Shape-Dependent Bkgd Modeling					
Signal σ				×	
Multijet					

Source	$H \rightarrow \gamma \gamma$	$H+X \rightarrow \tau \tau b \bar{b} / q \bar{q} \tau \tau$	$WH \rightarrow \tau \nu b \bar{b}$	$t \bar{t} H \rightarrow t \bar{t} b \bar{b}$
Luminosity	×	×	×	×
Normalization				
Jet Energy Scale		×	×	
Jet ID		×	×	
Tau Energy Scale/ID		×	×	
Electron ID/Trigger	×			
Muon ID/Trigger				
b -Jet Tagging			×	
Background σ		×	×	×
Background Modeling				
Signal σ	×			
Multijet				

TABLE V: Combined 95% C.L. limits on $\sigma \times BR(H \rightarrow b \bar{b} / W^+ W^-)$ for SM Higgs boson production. The limits are reported in units of the SM production cross section times branching fraction.

m_H (GeV/ c^2)	100	105	110	115	120	125	130	135	140	145	150
Expected:	2.4	2.4	3.0	3.1	3.8	4.0	4.1	4.3	3.9	3.5	2.9
Observed:	2.8	2.7	3.2	3.2	3.3	4.0	5.0	4.4	4.3	4.2	3.6

m_H (GeV/ c^2)	155	160	165	170	175	180	185	190	195	200
Expected:	2.5	1.8	1.7	2.0	2.5	2.8	4.1	4.9	5.9	6.6
Observed:	2.3	1.8	1.3	1.4	1.6	1.8	3.2	3.3	3.5	4.2

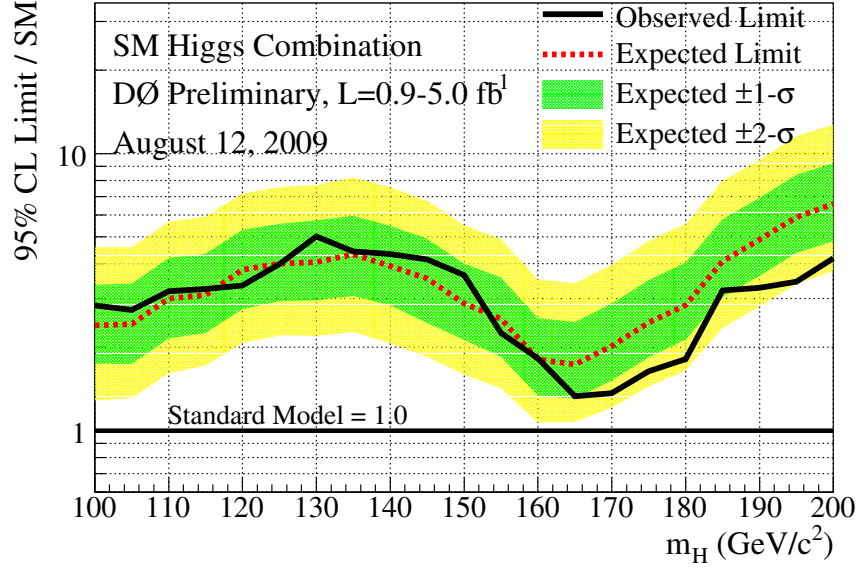


FIG. 5: Expected (median) and observed 95% C.L. cross section upper limit ratios for the combined $WH/ZH/H, H \rightarrow b\bar{b}/W^+W^-/\gamma\gamma/\tau^+\tau^-$ analyses over the $100 \leq m_H \leq 200$ GeV/c^2 mass range.

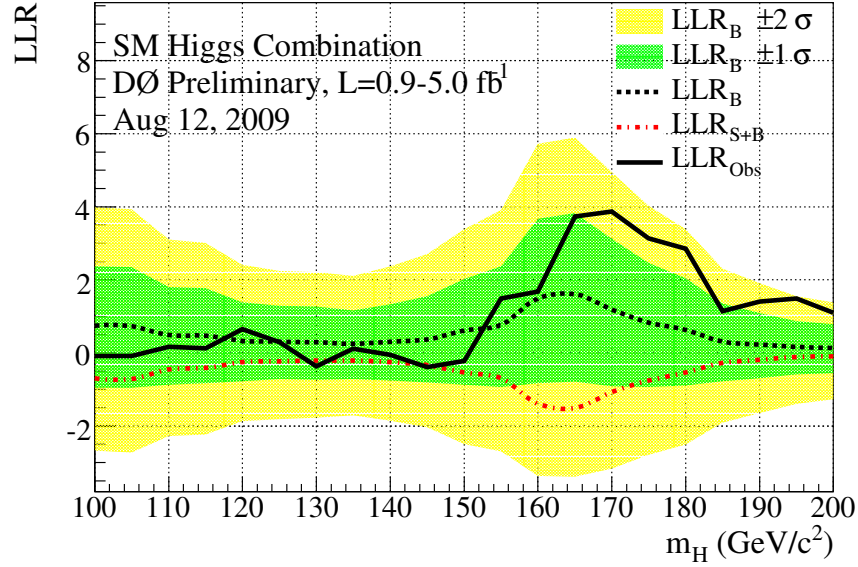


FIG. 6: Log-likelihood ratio distribution for the combined $WH/ZH/H, H \rightarrow b\bar{b}/W^+W^-/\gamma\gamma/\tau^+\tau^-$ analyses over the $100 \leq m_H \leq 200$ GeV/c^2 mass range.

-
- [1] R. Barate *et al.* [LEP Working Group for Higgs boson searches], Phys. Lett. B **565**, 61 (2003), [arXiv:hep-ex/0306033].
 - [2] LEP Electroweak Working Group: <http://lepewwg.web.cern.ch/LEPEWWG/plots/winter2009/>.
 - [3] DØ Collaboration, V. Abazov *et al.*, Nucl. Instrum. Meth. A **565**, 463 (2006) [arXiv:hep-ph/0507191].
 - [4] DØ Collaboration, DØ Note 5972-CONF.
 - [5] DØ Collaboration, DØ Note 5883-CONF.
 - [6] DØ Collaboration, DØ Note 5485-CONF.
 - [7] DØ Collaboration, DØ Note 5586-CONF.
 - [8] DØ Collaboration, DØ Note 5482-CONF.
 - [9] DØ Collaboration, DØ Note 5876-CONF.
 - [10] DØ Collaboration, DØ Note 5845-CONF.
 - [11] DØ Collaboration, DØ Note 5873-CONF.
 - [12] DØ Collaboration, DØ Note 5871-CONF.
 - [13] DØ Collaboration, DØ Note 5846-CONF.
 - [14] DØ Collaboration, DØ Note 5739-CONF.
 - [15] T. Scanlon, FERMILAB-THESIS-2006-43.
 - [16] DØ Collaboration, DØ Note 5902-CONF.
 - [17] T. Sjöstrand, P. Edén, C. Friberg, L. Lönnblad, G. Miu, S. Mrenna and E. Norrbin, Computer Phys. Commun. **135** 238 (2001) [arXiv:hep-ph/0010017].
 - [18] J. Pumplin *et al.*, JHEP **0207**, 012 (2002).
 - [19] S. Catani *et al.*, JHEP **0307**, 028 (2003) [arXiv:hep-ph/0306211].
 - [20] K. A. Assamagan *et al.* [Higgs Working Group Collaboration], arXiv:hep-ph/0406152.
 - [21] T. Hahn *et al.*, arXiv:hep-ph/0607308v2.
 - [22] D. de Florian and M. Grazzini, , arXiv:0901.2427v1 [hep-ph] (2009).
 - [23] A. D. Martin, W. J. Stirling, R. S. Thorne and G. Watt, arXiv:0901.0002 [hep-ph] (2009).
 - [24] U. Aglietti, R. Bonciani, G. Degrossi, A. Vicini, , arXiv:hep-ph/0610033v1 (2006).
 - [25] A. D. Martin, R. G. Roberts, W. J. Stirling and R. S. Thorne, Phys. Lett. B **531**, 216 (2002) [arXiv:hep-ph/0201127].
 - [26] A. Djouadi, J. Kalinowski and M. Spira, Comput. Phys. Commun. **108**, 56 (1998) [arXiv:hep-ph/9704448].
 - [27] M. L. Mangano *et al.*, JHEP **0307**, 001 (2003) [arXiv:hep-ph/0206293].
 - [28] A. Pukhov *et al.*, arXiv:hep-ph/9908288.
 - [29] <http://mcfm.fnal.gov/>.
 - [30] T. Junk, Nucl. Instrum. Meth. A **434**, 435 (1999); A.Read, CERN 2000-005 (30 May 2000).
 - [31] A. Read, Nucl. Instrum. Meth. A **425**, 357 (1999).
 - [32] W. Fisher, FERMILAB-TM-2386-E.